The Genetic Architecture of Multimodal Human Brain Age

Junhao Wen[1*], Bingxin Zhao[2], Zhijian Yang[3], Guray Erus[3], Ioanna Skampardoni[3], Elizabeth Mamourian[3], Yuhan Cui[3], Gyujoon Hwang[3], Jingxuan Bao[4], Aleix Boquet-Pujadas[5], Zhen Zhou[3], Yogasudha Veturi[6], Marylyn D. Ritchie[7], Haochang Shou[3], Paul M. Thompson[8], Li Shen[4], Arthur W. Toga[9], Christos Davatzikos[3]

[1]Laboratory of AI and Biomedical Science (LABS), Stevens Neuroimaging and Informatics Institute, Keck School of Medicine of USC, University of Southern California, Los Angeles, California, USA
[2]Department of Statistics and Data Science, University of Pennsylvania, Philadelphia, PA, USA
[3]Artificial Intelligence in Biomedical Imaging Laboratory (AIBIL), Center for AI and Data Science for Integrated Diagnostics (AI[2]D), Perelman School of Medicine, University of Pennsylvania, Philadelphia, USA
[4]Department of Biostatistics, Epidemiology and Informatics, University of Pennsylvania Perelman School of Medicine, Philadelphia, USA
[5]Biomedical Imaging Group, EPFL, Lausanne, Switzerland
[6]Department of Biobehavioral Health and Statistics, Penn State University, University Park, PA, USA
[7]Department of Genetics and Institute for Biomedical Informatics, Perelman School of Medicine, University of Pennsylvania, Philadelphia, PA, USA
[8]Imaging Genetics Center, Mark and Mary Stevens Neuroimaging and Informatics Institute, Keck School of Medicine of USC, University of Southern California, Marina del Rey, California
[9]Laboratory of Neuro Imaging (LONI), Stevens Neuroimaging and Informatics Institute, Keck School of Medicine of USC, University of Southern California, Los Angeles, California, USA

[*]Corresponding author:
Junhao Wen, junhaowe@usc.edu
2025 Zonal Ave, Los Angeles, CA 90033, United States

Word counts: 4514 words

Abstract

The complex biological mechanisms underlying human brain aging remain incompletely understood, involving multiple body organs and chronic diseases. In this study, we used multimodal magnetic resonance imaging and artificial intelligence to examine the genetic architecture of the brain age gap (BAG) derived from gray matter volume (GM-BAG, *N*=31,557 European ancestry), white matter microstructure (WM-BAG, *N*=31,674), and functional connectivity (FC-BAG, *N*=32,017). We identified sixteen genomic loci that reached genome-wide significance (P-value<$5x10^{-8}$). A gene-drug-disease network highlighted genes linked to GM-BAG for treating neurodegenerative and neuropsychiatric disorders and WM-BAG genes for cancer therapy. GM-BAG showed the highest heritability enrichment for genetic variants in conserved regions, whereas WM-BAG exhibited the highest heritability enrichment in the 5' untranslated regions; oligodendrocytes and astrocytes, but not neurons, showed significant heritability enrichment in WM and FC-BAG, respectively. Mendelian randomization identified potential causal effects of several exposure variables on brain aging, such as type 2 diabetes on GM-BAG (odds ratio=1.05 [1.01, 1.09], P-value=$1.96x10^{-2}$) and AD on WM-BAG (odds ratio=1.04 [1.02, 1.05], P-value=$7.18x10^{-5}$). Overall, our results provide valuable insights into the genetics of human brain aging, with clinical implications for potential lifestyle and therapeutic interventions. All results are publicly available at the MEDICINE knowledge portal: https://labs.loni.usc.edu/medicine.

Main

The advent of artificial intelligence (AI) has provided novel approaches to investigate various aspects of human brain health[1,2], such as normal brain aging[3], neurodegenerative disorders such as Alzheimer's disease (AD)[4], and brain cancer[5]. Based on magnetic resonance imaging (MRI), AI-derived measures of the human brain age[6–8] have emerged as a valuable biomarker for evaluating brain health. More precisely, the difference between an individual's AI-predicted brain age and chronological age – brain age gap (BAG) – provides a means of quantifying an individual's brain health by measuring deviation from the normative aging trajectory. BAG has demonstrated sensitivity to several common brain diseases, clinical variables, and cognitive functions[9], presenting the promising potential for its use in the general population to capture relevant pathological processes.

Brain imaging genomics[10], an emerging scientific field advanced by both computational statistics and AI, uses imaging-derived phenotypes (IDP[11]) from MRI and genetics to offer mechanistic insights into healthy and pathological aging of the human brain. Recent large-scale genome-wide association studies (GWAS)[11–18] have identified a diverse set of genomic loci linked to gray matter (GM)-IDP from T1-weighted MRI, white matter (WM)-IDP from diffusion MRI [fractional anisotropy (FA), mean diffusivity (MD), neurite density index (NDI), and orientation dispersion index (ODI)], and functional connectivity (FC)-IDP from functional MRI. While previous GWAS[19] have associated BAG with common genetic variants [e.g., single nucleotide polymorphism (SNP)], they primarily focused on GM-BAG[9,20–22] or did not comprehensively capture the genetic architecture of the multimodal BAG[19] via post-GWAS analyses in order to biologically validate the GWAS signals. It is crucial to holistically identify the genetic factors associated with multimodal BAGs (GM, WM, and FC-BAG), where each

BAG reflects distinct and/or similar neurobiological facets of human brain aging. Furthermore, dissecting the genetic architecture of human brain aging may determine the causal implications, which is essential for developing gene-inspired therapeutic interventions. Finally, numerous risk or protective lifestyle factors and neurobiological processes may also exert independent, synergistic, antagonistic, sequential, or differential influences on human brain health. Therefore, a holistic investigation of multimodal BAGs is urgent to fully capture the genetics of human brain aging, including the genetic correlation, gene-drug disease network, and potential causality. In this study, we postulate that AI-derived GM, WM, and FC-BAG can serve as robust, complementary endophenotypes[23] – close to the underlying etiology – for precise quantification of human brain health.

The present study sought to uncover the genetic architecture of multimodal BAG and explore the causal relationships between protective/risk factors and decelerated/accelerated brain age. To accomplish this, we analyzed multimodal brain MRI scans from 42,089 participants from the UK Biobank (UKBB) study[24] and used 119 GM-IDP, 48 FA WM-IDP, and 210 FC-IDP to derive GM, WM, and FC-BAG, respectively. Refer to **Method 1** for selecting the final feature sets for each BAG. We first compared the age prediction performance of different machine learning models using these IDPs. We then performed GWAS to identify genomic loci associated with GM, WM, and FC-BAG in the European ancestry population. In post-GWAS analyses, we constructed a gene-drug-disease network, estimated the genetic correlation with several brain disorders, assessed their heritability enrichment in various functional categories or specific cell types, and calculated the polygenic risk scores (PRS) of the three BAGs. Finally, we performed Mendelian Randomization (MR)[25] to infer the causal effects of several clinical traits and diseases on the three BAGs.

Results

In the first section, we objectively compared the age prediction performance of four machine learning methods using these GM, WM, and FC-IDPs (**Fig. 1A**). To this end, we employed a nested cross-validation (CV) procedure in the training/validation/test dataset (N=4000); an independent test dataset (N=38,089)[26,27] was held out – unseen until we finalized the models using only the training/validation/test dataset (**Method 1**). The four machine learning models included support vector regression (SVR), LASSO regression, multilayer perceptron (MLP), and a five-layer neural network (i.e., three linear layers and one rectified linear unit layer; hereafter, NN)[28] (**Method 3**). The second section focused on the main GWASs using the European ancestry population (31,557<N<32,017) and their sensitivity checks in six scenarios (**Method 4A**). In the last section, we validated the GWAS findings in several post-GWAS analyses, including genetic correlation, gene-drug-disease network, partitioned heritability, PRS calculation, and Mendelian randomization (**Method 4**).

GM, WM, and FC-BAG derived from three MRI modalities

Several findings were observed based on the results from the independent test dataset (N=38,089, **Method 1**). First, GM-IDP (4.39<mean absolute error (MAE)<5.35; 0.64<r<0.66), WM-IDP (4.92<MAE<7.95; 0.42<r<0.65), and FC-IDP (5.48<MAE<6.05; 0.43 <r<0.46) achieved gradually a higher MAE and smaller Pearson's correlation (r) (**Fig. 1B**, **C**, and **D**). Second, LASSO regression obtained the lowest MAE for GM, WM, and FC-IDP; linear models obtained a lower MAE than non-linear networks (**Fig. 1B**). Third, all models generalized well from the training/validation/test dataset (N=4000, **Method 1**) to the independent test dataset. However, simultaneously incorporating WM-IDP from FA, MD, NDI, and ODI resulted in severely

overfitting models (**Supplementary eTable 1A**). The observed overfitting may be attributed to many parameters (*N*=38,364) in the network or strong correlations among the diffusion metrics (i.e., FA, MD, ODI, and NDI). Fourth, the experiments stratified by sex did not exhibit substantial differences, except for a stronger overfitting tendency observed in females compared to males using WM-IDP incorporating the four diffusion metrics (**Supplementary eTable 1B**). Detailed results of the CV procedure, including the training, validation, test performance, and sex-stratified experiments, are presented in **Supplementary eTable 1**. In all subsequent genetic analyses, we reported the results using BAG derived from the three LASSO models with the lowest MAE in each modality (**Fig. 1A**), with the "age bias" corrected as in De Lange et al.[29].

In the literature, other studies[30–33] have thoroughly evaluated age prediction performance using different machine learning models and input features. More et al.[34] systematically compared the performance of age prediction of 128 workflows (MAE between 5.23–8.98 years) and showed that voxel-wise feature representation (MAE approximates 5-6 years) outperformed parcel-based features (MAE approximates 6-9 years) using conventional machine learning algorithms (e.g., LASSO regression). Using deep neural networks, Peng et al.[30] and Leonardsen et al.[31] reported a lower MAE (nearly 2.5 years) with voxel-wise imaging scans. However, we previously showed that a moderately fitting convolutional neural network (CNN) obtained significantly higher differentiation (a larger effect size) than a tightly fitting CNN (a lower MAE) between the disease and health groups[35]. To summarize, our study's brain age prediction performance aligns with those reported in the existing literature, considering the utilization of low-dimensional hand-crafted IDPs and conventional machine learning algorithms[34].

Finally, we calculated the phenotypic correlation (p_c) between GM, WM, and FC-BAG using Pearson's correlation coefficient. GM-BAG and WM-BAG showed the highest positive

141 correlation (p_c=0.38; P-value<1x10^{-10}; N=30,733); GM-BAG (p_c=0.09; P-value<1x10^{-10};

142 N=30,660) and WM-BAG (p_c=0.10; P-value<1x10^{-10}; N=31,574) showed weak correlations with

143 FC-BAG (**Fig. 1E**).

144

Figure 1: **Brain age prediction using three MRI modalities and four machine learning models**

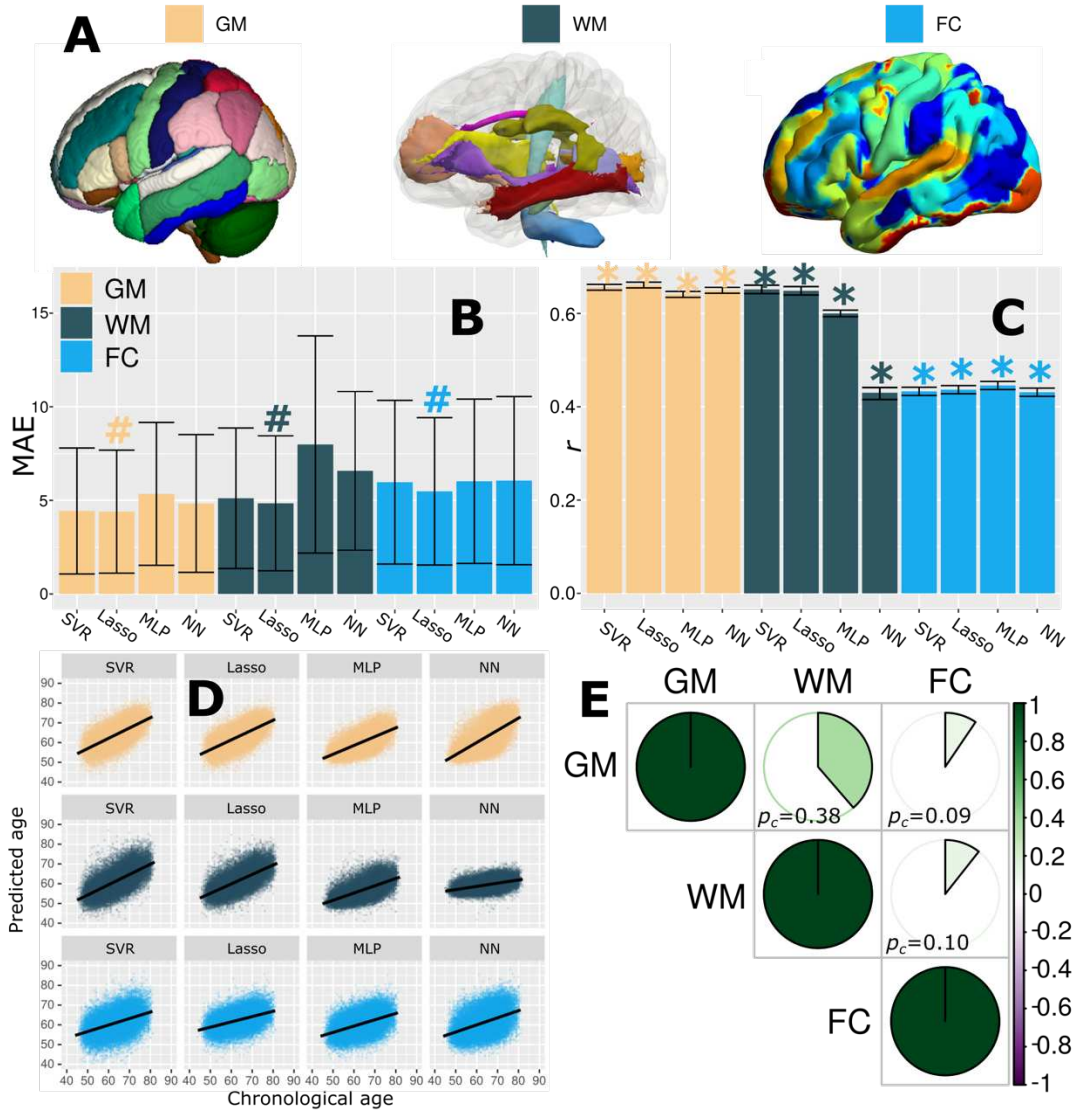

A) Multimodal brain MRI data were used to derive imaging-derived phenotypes (IDP) for T1-weighted MRI (119 GM-IDP), diffusion MRI (48 WM-IDP), and resting-state functional MRI (210 FC-IDP). IDPs for each modality are shown here using different colors based on predefined brain atlases or ICA for FC-IDP. **B**) Linear models achieved lower mean absolute errors (MAE) than non-linear models using support vector regression (SVR), LASSO regression, multilayer perceptron (MLP), and a five-layer neural network (NN). The MAE for the independent test dataset is presented, and the # symbol indicates the model with the lowest MAE for each modality. Error bars represent standard deviation (SD). **C**) Pearson's correlation (*r*) between the predicted brain age and chronological age is computed, and statistical significance (P-value<0.05) - after adjustment for multiple comparisons using the FDR method - is denoted by the * symbol. Error bars represent the 95% confidence interval (CI). **D**) Scatter plot for the predicted brain age and chronological age. **E**) Phenotypic correlation (p_c) between the GM, WM, and FC-BAG using Pearson's correlation coefficient (*r*).

GM, WM, and FC-BAG are associated with sixteen genomic loci

In the European ancestry populations, GWAS (**Method 4A**) revealed 6, 9, and 1 genomic loci linked to GM (N=31,557), WM (N=31,674), and FC-BAG (N=32,017), respectively (**Fig. 2A**). The top lead SNP and mapped genes of each locus are presented in **Supplementary eTable 2**. We also calculated the genomic inflation factor (λ) and the linkage disequilibrium score regression (LDSC) intercept (b)[36] to scrutinize the robustness of the GWAS of GM-BAG (λ=1.118; b=1.0016±0.0078), WM-BAG (λ=1.124; b=1.0187±0.0073), and FC-BAG (λ=1.046; b=1.0039±0.006). All LDSC intercepts were close to 1, indicating no substantial genomic inflation. The individual Manhattan and QQ plots of the three GWASs are presented in **Supplementary eFigure 3** and are also publicly available at the MEDICINE knowledge portal: https://labs.loni.usc.edu/medicine. The three BAGs were significantly heritable (P-value<1×10^{-10}) after adjusting for multiple comparisons using the Bonferroni method using the genome-wide complex trait analysis (GCTA) software[37]. GM-BAG showed the highest SNP-based heritability (h^2=0.47±0.02), followed by WM-BAG (h^2=0.46±0.02) and FC-BAG (h^2=0.11±0.02).

We performed a query in the GWAS Catalog[38] for these genetic variants within each locus to understand the phenome-wide association of these identified loci in previous literature (**Method 4C**). Notably, the SNPs within each locus were linked to other traits previously reported in the literature (**Supplementary eFile 1**). Specifically, the GM-BAG loci were uniquely associated with neuropsychiatric disorders such as major depressive disorder (MDD), heart disease, and cardiovascular disease. We also observed associations between these loci and other diseases (including anemia), as well as biomarkers from various human organs (e.g., liver) (**Fig. 2B**). We then performed positional and functional annotations to map SNPs to genes associated with GM, WM, and FC-BAG loci (**Method 4B**). **Fig. 2C-E** showcased the regional

Manhattan plot of one genomic locus linked to GM, WM, and FC-BAG. A detailed discussion of these exemplary loci, SNPs, and genes is presented in **Supplementary eText 1**.

Finally, we calculated the genetic correlation (g_c) between the GM, WM, and FC-BAG using the LDSC software. GM-BAG and WM-BAG showed the highest positive correlation (g_c=0.49; P-value<$1x10^{-10}$); GM-BAG (g_c=0.20; P-value=0.025) and WM-BAG (g_c=0.29; P-value=0.005) showed weak correlations with FC-BAG (**Fig. 2F**). The genetic correlations largely mirror the phenotypic correlations, supporting the long-standing Cheverud's Conjecture[39]. We also verified that these genetic correlations exhibited consistency between the two random splits (split1 and spit2: 15,778<*N*<16,008), sharing a similar age and sex distribution (**Supplementary eFigure 2**).

Sensitivity analyses for the genome-wide associations

We aimed to check the robustness of the main GWASs using the full sample sizes of the European populations (**Fig. 2A**). To this end, we performed six sensitivity analyses (**Method 4A**).

Applying the Bonferroni method to correct for multiple comparisons, we noted high concordance rates between the split1 (as discovery, 15,778<*N*<16,008) and split2 (as replication, 15,778<*N*<16,008) GWASs. Specifically, for GM-BAG, we observed a concordance rate of 99% [P-value<0.05/3092; 3092 significant SNPs passing the genome-wide P-value threshold (<$5x10^{-8}$) in the discovery data], and for WM-BAG, the concordance rate reached 100% (P-value<0.05/116). FC-BAG did not achieve significant genome-wide results in the spit-sample GWASs (**Supplementary eFigure 3** and **Supplementary eFile 2**).

In sex-stratified GWASs, the concordance rates were 100% (P-value<0.05/3072) for GM-BAG and 88.6% (P-value<0.05/116) for WM-BAG when comparing the male-GWAS (as replication, 14,969<*N*<15,127) to female-GWAS (as discovery, 16,588<*N*<16,890). FC-BAG did not achieve significant genome-wide results (**Supplementary eFigure 4** and **Supplementary eFile 3**).

The concordance rates of the GWASs using non-European ancestry populations (as replication, 4646<*N*<5091) were low compared to the main GWASs using the European population: only 13.78% for GM-BAG and 41.94% for WM-BAG (P-value<0.05) (**Supplementary eFigure 5** and **Supplementary eFile 4**).

A mixed linear model employed via fastGWA[40] (as replication, 31,557<*N*<32,017) obtained 100% concordance rates for GM, WM, and FC-BAG compared to GWAS using PLINK linear regression (**Supplementary eFile 5**). The genetic loci, genomic inflation factor (λ), and the LDSC intercepts for GM, WM, and FC-BAG were similar between the PLINK and fastGWA analyses (**Supplementary eFigure 6**).

We found a 100% concordance rate of the SNPs identified for the GM-BAG GWAS using LASSO regression (as discovery, BAG MAE=4.39 years) and SVR (P-value < 0.05/3382, as replication, BAG MAE=4.43 years) (**Supplementary eFigure 7** and **Supplementary eFile 6**). The BAGs derived from the two machine larning models were highly correlated (r=0.99; P-value<$1x10^{-10}$).

We finally found a 92.43% concordance rate of the SNPs identified in the GM-BAG GWAS using the 119 MUSE ROIs[41] (as discovery, BAG MAE=4.39 years) and voxel-wide RAVENS[42] maps (as replication, P-value < 0.05/3382, BAG MAE=5.12 years) (**Supplementary eFigure 8** and **Supplementary eFile 7**). The BAGs derived from the two types of features were

significantly correlated (r=0.74; P-value<$1x10^{-10}$). The brain age prediction performance using RAVENS showed marginal overfitting, with an MAE of 4.31 years in the training/validation/test dataset and an MAE of 5.12 years in the independent test dataset.

These findings suggest that our GWASs were robust across sex, random splits, imaging features, GWAS methods, and machine learning methods within European populations; however, their generalizability to non-European populations is limited. All subsequent post-GWAS analyses were conducted using the main GWAS results of European ancestry.

Figure 2: **Genome-wide associations of multimodal brain age gaps**

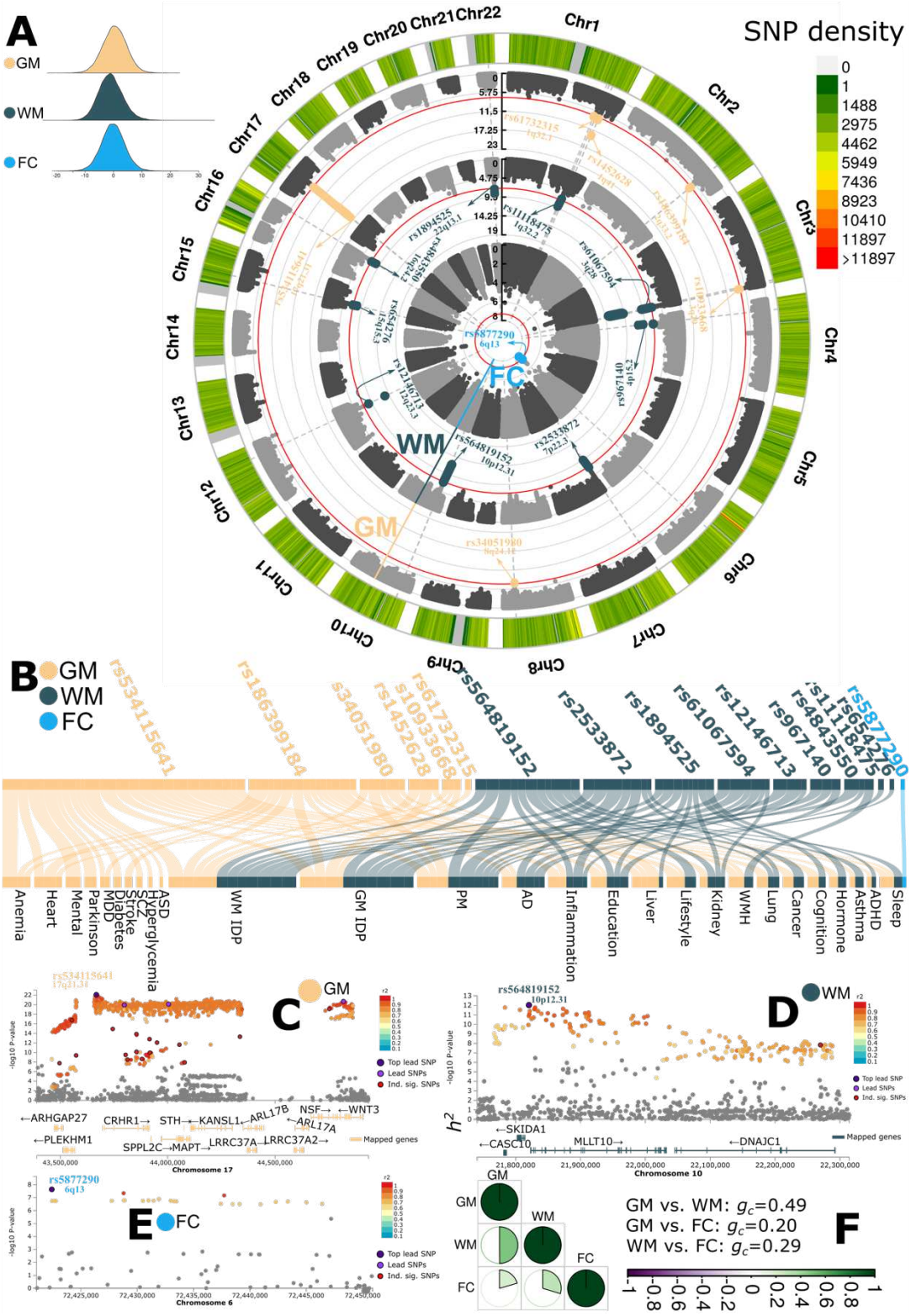

A) Genome-wide associations identified sixteen genomic loci associated with GM (6), WM (9), and FC-BAG (1) using a genome-wide P-value threshold [$-\log_{10}$(P-value) > 7.30]. The top lead

SNP and the cytogenetic region number represent each locus. **B**) Phenome-wide association query from GWAS Catalog[38]. Independent significant SNPs inside each locus were largely associated with many traits. We further classified these traits into several trait categories, including biomarkers from multiple body organs (e.g., heart and liver), neurological disorders (e.g., Alzheimer's disease and Parkinson's disease), and lifestyle risk factors (e.g., alcohol consumption). **C**) Regional plot for a genomic locus associated with GM-BAG. Color-coded SNPs are decided based on their highest r^2 to one of the nearby independent significant SNPs. Gray-colored SNPs are below the r^2 threshold. The top lead SNP, lead SNPs, and independent significant SNPs are denoted as dark purple, purple, and red, respectively. Mapped, orange-colored genes of the genomic locus are annotated by positional, eQTL, and chromatin interaction mapping (**Method 4B**). **D**) Regional plot for a genomic locus associated with WM-BAG. **E**) The novel genomic locus associated with FC-BAG did not map to any genes. We used the Genome Reference Consortium Human Build 37 (GRCh37) in all genetic analyses. **F**) Genetic correlation (g_c) between the GM, WM, and FC-BAG using the LDSC software. Abbreviation: AD: Alzheimer's disease; ASD: autism spectrum disorder; PD: Parkinson's disease; ADHD: attention-deficit/hyperactivity disorder.

The gene-drug-disease network highlights disease-specific drugs that bind to genes associated with GM and WM-BAG

We investigated the potential "druggable genes[43]" from the mapped genes by constructing a gene-drug-disease network (**Method 4F**). The network connects genes with drugs (or drug-like molecules) targeting specific diseases currently active at any stage of clinical trials.

We revealed clinically relevant associations for 4 and 6 mapped genes associated with GM-BAG and WM-BAG, respectively. The GM-BAG genes were linked to clinical trials for treating heart, neurodegenerative, neuropsychiatric, and respiratory diseases. On the other hand, the WM-BAG genes were primarily targeted for various cancer treatments and cardiovascular diseases (**Fig. 3**). To illustrate, for the GM-BAG *MAPT* gene, several drugs or drug-like molecules are currently being evaluated for treating AD. Semorinemab (RG6100), an anti-tau IgG4 antibody, was being investigated in a phase-2 clinical trial (trial number: NCT03828747), which targets extracellular tau in AD, to reduce microglial activation and inflammatory responses[44]. Another drug is the LMTM (TRx0237) - a second-generation tau protein

aggregation inhibitor currently being tested in a phase-3 clinical trial (trial number: NCT03446001) for treating AD and frontotemporal dementia[45]. Regarding WM-BAG genes, they primarily bind with drugs for treating cancer and cardiovascular diseases. For instance, the *PDIA3* gene, associated with the folding and oxidation of proteins, has been targeted for developing several zinc-related FDA-approved drugs for treating cardiovascular diseases. Another example is the *MAP1A* gene, which encodes microtubule-associated protein 1A. This gene is linked to the development of estramustine, an FDA-approved drug for prostate cancer (**Fig. 3**). Detailed results are presented in **Supplementary eFile 8**.

Figure 3: **Gene-drug-disease network of multimodal brain age gaps**

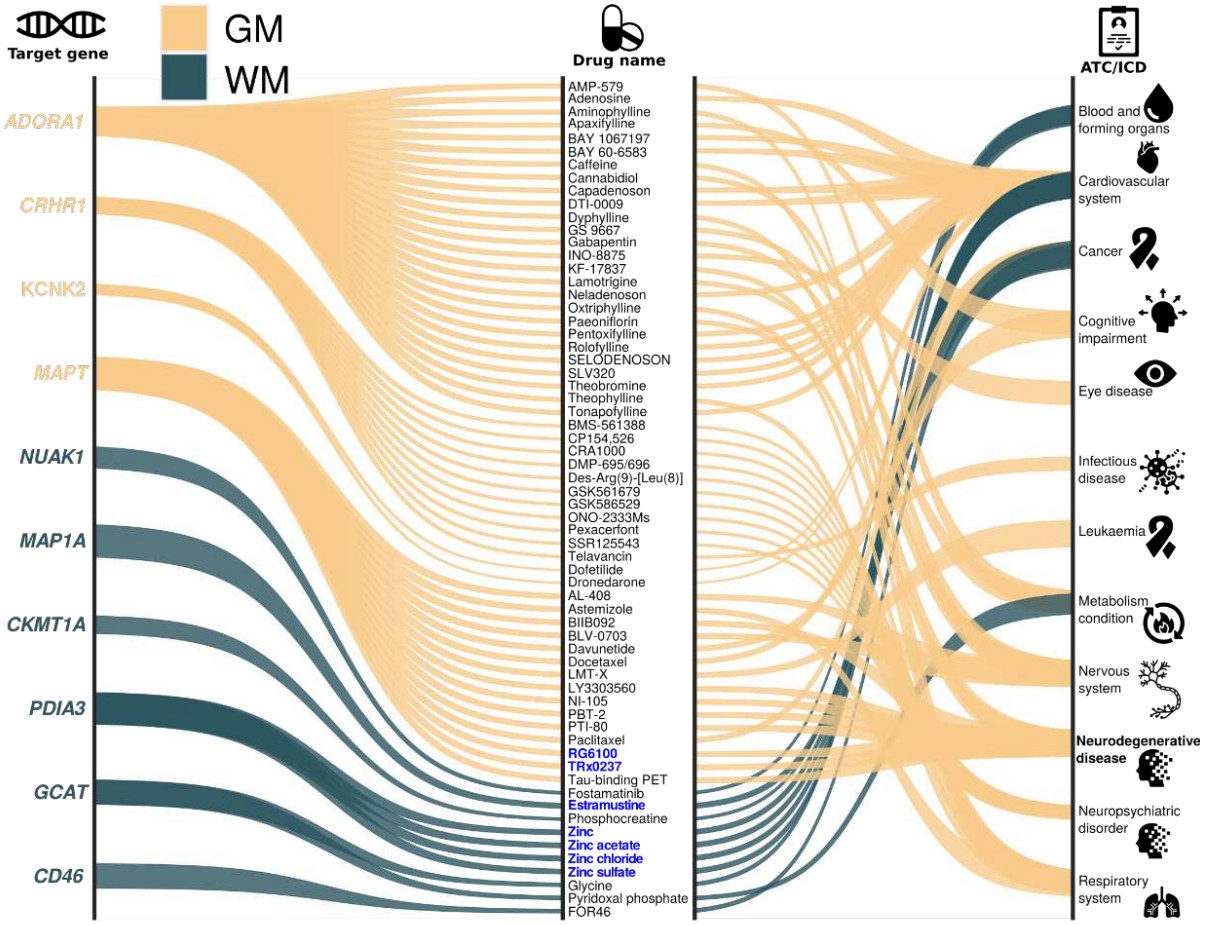

The gene-drug-disease network derived from the mapped genes revealed a broad spectrum of targeted diseases and cancer, including brain cancer, cardiovascular system diseases, Alzheimer's disease, and obstructive airway disease, among others. The thickness of the lines represented the P-values ($-\log_{10}$) from the brain tissue-specific gene set enrichment analyses using the GTEx v8 dataset. We highlight several drugs under the blue-colored and bold text. Abbreviation: ATC: Anatomical Therapeutic Chemical; ICD: International Classification of Diseases.

Multimodal BAG is genetically correlated with AI-derived subtypes of brain diseases

We calculated the genetic correlation using the GWAS summary statistics from 16 clinical traits to examine genetic covariance between multimodal BAG and other clinical traits. The selection procedure and quality check of the GWAS summary statistics are detailed in **Method 4D**. These traits encompassed common brain diseases and their AI-derived disease subtypes, as well as education and intelligence (**Fig. 4A** and **Supplementary eTable 3**). The AI-generated disease

295 subtypes were established in our previous studies utilizing semi-supervised clustering methods[46]
296 and IDP from brain MRI scans.

297 Our analysis revealed significant genetic correlations between GM-BAG and AI-derived
298 subtypes of AD (AD1[4]), autism spectrum disorder (ASD) (ASD1 and ASD3[47]), schizophrenia
299 (SCZ1[48]), and obsessive-compulsive disorder (OCD)[49]; WM-BAG and AD1, ASD1, SCZ1, and
300 SCZ2; and FC-BAG and education[50] and SCZ1. Detailed results for r_g estimates are presented in
301 **Supplementary eTable 4**. These subtypes, in essence, capture more homogeneous disease
302 effects than the conventional "unitary" disease diagnosis, hence serving as robust
303 endophenotypes[23].

304

305 **Multimodal BAG shows specific enrichment of heritability in different functional**
306 **categories and cell types**

307 We conducted a partitioned heritability analysis[51] to investigate the heritability enrichment of
308 genetic variants related to multimodal BAG in the 53 functional categories (**Method 4E**). Our
309 results revealed that GM and WM-BAG exhibited significant heritability enrichment across
310 numerous annotated functional categories. Specifically, some categories displayed greater
311 enrichment than others, and we have outlined some in further detail.

312 For GM-BAG, the regions conserved across mammals, as indicated by the label
313 "conserved" in **Fig. 4B**, displayed the most notable enrichment of heritability: approximately
314 2.61% of SNPs were found to explain 0.43±0.07 of SNP heritability (P-value=5.80×10^{-8}).
315 Additionally, transcription start site (TSS)[52] regions employed 1.82% of SNPs to explain
316 0.16±0.05 of SNP heritability (P-value=8.05×10^{-3}). TSS initiates the transcription at the 5' end of
317 a gene and is typically embedded within a core promoter crucial to the transcription machinery[53].

The heritability enrichment of Histone H3 at lysine 4, as denoted for "H3K4me3_peaks" in **Fig. 4B**, and histone H3 at lysine 9 (H3K9ac)[54] were also found to be large and were known to highlight active gene promoters[55]. For WM-BAG, 5' untranslated regions (UTR) used 0.54% of SNPs to explain 0.09±0.03 of SNP heritability (P-value=4.24×10^{-3}). The 5' UTR is a crucial region of a messenger RNA located upstream of the initiation codon. It is pivotal in regulating transcript translation, with varying mechanisms in viruses, prokaryotes, and eukaryotes.

Additionally, we examined the heritability enrichment of multimodal BAG in three different cell types (**Fig. 4C**). WM-BAG (P-value=1.69×10^{-3}) exhibited significant heritability enrichment in oligodendrocytes, one type of neuroglial cells. FC-BAG (P-value=1.12×10^{-2}) showed such enrichment in astrocytes, the most prevalent glial cells in the brain. GM-BAG showed no enrichment in any of these cells. Our findings are consistent with understanding the molecular and biological characteristics of GM and WM. Oligodendrocytes are primarily responsible for forming the lipid-rich myelin structure, whereas astrocytes play a crucial role in various cerebral functions, such as brain development and homeostasis. Convincingly, a prior GWAS[14] on WM-IDP also identified considerable heritability enrichment in glial cells, especially oligodendrocytes. Detailed results for the 53 functional categories and cell-specific analyses are presented in **Supplementary eTable 5**.

Prediction ability of the polygenic risk score of the multimodal BAG

We derived the PRS for GM, WM, and FC-BAG using the conventional C+T (clumping plus P-value threshold) approach[56] via PLINK and a Bayesian method via PRS-CS[57] (**Method 4H**).

We found that the GM, WM, and FC-BAG-PRS derived from PRS-CS significantly predicted the phenotypic BAGs in the test data (split2 GWAS, $15{,}697<N<15{,}940$), with an

incremental R^2 of 2.17%, 1.85%, and 0.19%, respectively (**Fig. 4D**). Compared to the PRS derived from PRS-CS, the PLINK approach achieved a lower incremental R^2 of 0.81%, 0.45%, and 0.14% for GM, WM, and FC-BAG, respectively (**Supplementary eFigure 9**). Overall, the predictive capacity of PRS is moderate, in line with earlier discoveries involving raw imaging-derived phenotypes, as demonstrated in Zhao et al.[13], where PRSs developed for seven selective brain regions were able to explain roughly 1.18% to 3.93% of the phenotypic variance associated with these traits.

Figure 4: **Genetic correlation, partitioned heritability enrichment, and PRS prediction accuracy on multimodal brain age gaps**

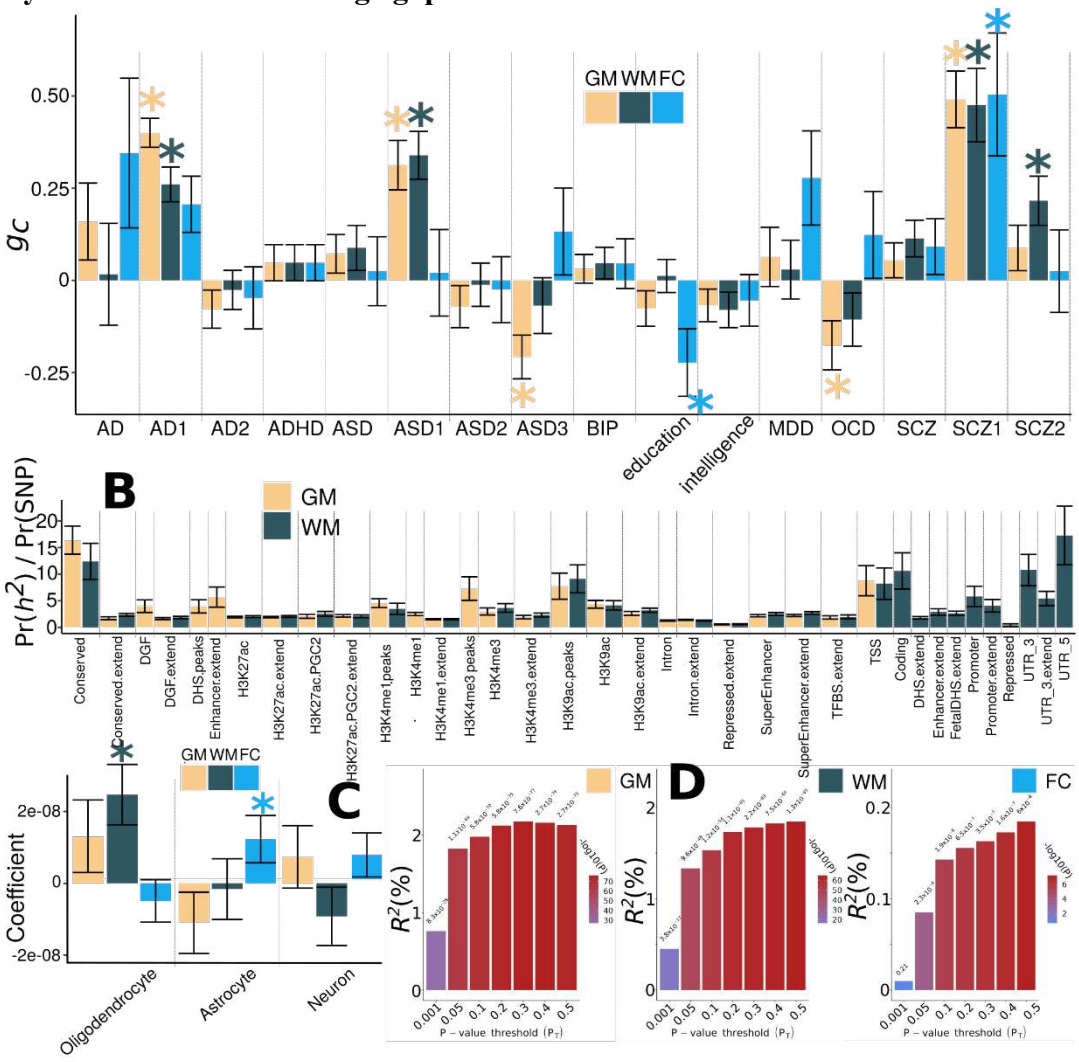

A) Genetic correlation (g_c) between GM, WM, and FC-BAG and 16 clinical traits. These traits include neurodegenerative diseases (e.g., AD) and their AI-derived subtypes (e.g., AD1 and AD2[4]), neuropsychiatric disorders (e.g., ASD) and their subtypes (ASD1, 2, and 3[47]), intelligence, and education. **B**) The proportion of heritability enrichment for the 53 functional categories[51]. We only show the functional categories that survived the correction for multiple comparisons using the FDR method. **C**) Cell type-specific partitioned heritability estimates. We included gene sets from Cahoy et al.[58] for three main cell types (i.e., astrocyte, neuron, and oligodendrocyte). After adjusting for multiple comparisons using the FDR method, the * symbol denotes statistical significance (P-value<0.05). Error bars represent the standard error of the estimated parameters. **D**) The incremental R^2 of the PRS derived by PRC-CS to predict the GM, WM, and FC-BAG in the target/test data (i.e., the split2 GWAS). The *y*-axis indicates the proportions of phenotypic variation (GM, WM, and FC-BAG) that the PRS can significantly and additionally explain. The *x*-axis lists the seven P-value thresholds considered. Abbreviation: AD: Alzheimer's disease; ADHD: attention-deficit/hyperactivity disorder; ASD: autism spectrum disorder; BIP: bipolar disorder; MDD: major depressive disorder; OCD: obsessive-compulsive disorder; SCZ: schizophrenia; CAD: coronary artery disease; CD: Crohn's disease; BMD: bone

mineral density; PD: Parkinson's disease; SLE: systemic lupus erythematosus; BMI: body mass index; CVD: cardiovascular disease; LDL: low-density lipoprotein cholesterol; MS: multiple sclerosis; AF: Atrial fibrillation.

The potential causal relationships between GM and WM-BAG and other clinical traits

We investigated the potential causal effects of several risk factors (i.e., exposure variable) on multimodal BAG (i.e., outcome variable) using a bidirectional two-sample MR approach[59] (**Method 4G**). We hypothesized that several diseases and lifestyle risk factors might contribute to accelerating or decelerating human brain aging.

We found putative causal effects of triglyceride-to-lipid ratio in very large very-low-density lipoprotein (VLDL)[60] [P-value=5.09×10^{-3}, OR (95% CI) = 1.08 (1.02, 1.13), number of SNPs=52], type 2 diabetes[61] [P-value=1.96×10^{-2}, OR (95% CI) = 1.05 (1.01, 1.09), number of SNPs=10], and breast cancer[62] [P-value=1.81×10^{-2}, OR (95% CI) = 0.96 (0.93, 0.99), number of SNPs=118] on GM-BAG (i.e., accelerated brain age). We also identified causal effects of AD[63] [P-value=7.18×10^{-5}, OR (95% CI) = 1.04 (1.02, 1.05), number of SNPs=13] on WM-BAG (**Fig. 5A**). We subsequently examined the potential inverse causal effects of multimodal BAG (i.e., exposure) on these risk factors (i.e., outcome). However, owing to the restricted power [number of instrumental variables (IV) < 6], we did not observe any significant signals (**Supplementary eFigure 10** and **Supplementary eFile 9**).

Sensitivity analyses for Mendelian randomization

We performed sensitivity analyses to investigate potential violations of the three IV assumptions (**Method 4G**). To illustrate this, we showcased the sensitivity analysis results for the causal effect of the triglyceride-to-lipid in VLDL ratio on GM-BAG (**Fig. 5B-E**). In a leave-one-out analysis, we found that no single SNP overwhelmingly drove the overall effect (**Fig. 5B**). There

was evidence for the presence of minor heterogeneity[64] of the causal effect amongst SNPs (Cochran's Q value=76.06, P-value=5.09×10^{-3}). Some SNPs exerted opposite causal effects compared to the model using all SNPs (**Fig. 5C**). The scatter plot (**Fig. 5D**) indicated one obvious SNP outlier (rs11591147), and the funnel plot showed little asymmetry with only an outlier denoted in **Fig. 5E** (rs4507142). Finally, the MR Egger estimator allows for pleiotropic effects independent of the effect on the exposure of interest (i.e., the InSIDE assumption[65]). Our results from the Egger estimator showed a small positive intercept ($5.21\times10^{-3}\pm2.87\times10^{-3}$, P-value=0.07) and a lower OR [inverse-variance weighted (IVW): 1.08 (1.02, 1.13) vs. Egger: 1.01 (0.93, 1.10)], which may indicate the presence of directional horizontal pleiotropy for some SNPs. We present sensitivity analyses for other significant exposure variables in **Supplementary eFigure 11**.

To investigate the potential directional pleiotropic effects, we re-analyzed the MR Egger regression by excluding the two outliers identified in **Fig. 5D** (rs11591147) and **E** (rs4507142), which led to a slightly increased OR [1.04 (0.96, 1.12)] and a smaller positive intercept ($4.41\times10^{-3}\pm2.65\times10^{-3}$, P-value=0.09). Our findings support that these two outlier SNPs may have a directional pleiotropic effect on GM-BAG. Nevertheless, given the complex nature of brain aging, many other biological pathways may also contribute to human brain aging. For instance, the SNP (rs11591147) was largely associated with other blood lipids, such as LDL cholesterol[66], and heart diseases, such as coronary artery disease[67]. Detailed results obtained from all five MR methods are presented in **Supplementary eFile 9**.

Figure 5: **Causal inference of multimodal brain age gaps**

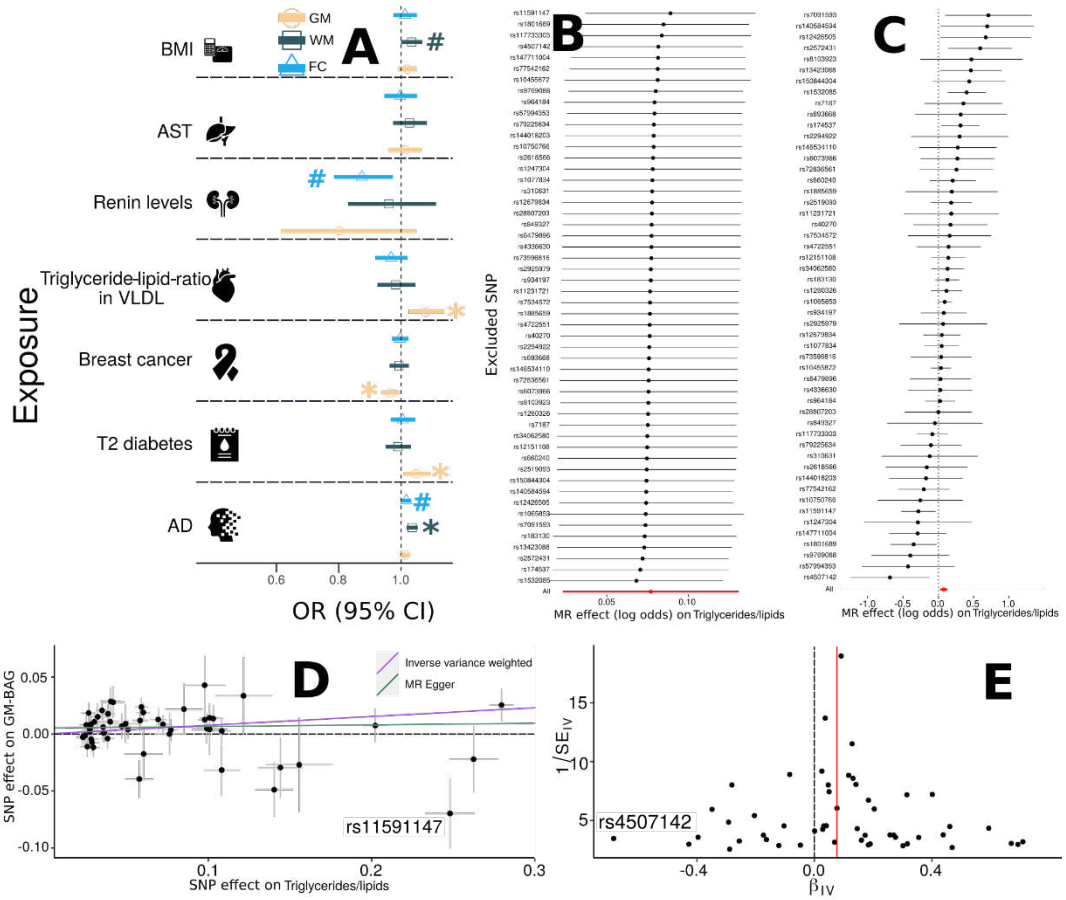

A) Causal inference was performed using a two-sample Mendelian Randomization (MR, **Method 4G**) approach for seven selected exposure variables on three outcome variables (i.e., GM, WM, and FC-BAG). The symbol * denotes statistical significance after correcting for multiple comparisons using the FDR method (*N*=7); the symbol # denotes the tests passing the nominal significance threshold (P-value=0.05) but did not survive the multiple comparisons. The odds ratio (OR) and the 95% confidence interval (CI) are presented. **B**) Leave-one-out analysis of the triglyceride-to-lipid ratio on GM-BAG. Each row represents the MR effect (log OR) and the 95% CI by excluding that SNP from the analysis. The red line depicts the IVW estimator using all SNPs. **C**) Forest plot for the single-SNP MR results. Each line represents the MR effect (log OR) for the triglyceride-to-lipid ratio on GM-BAG using only one SNP; the red line shows the MR effect using all SNPs together. **D**) Scatter plot for the MR effect sizes of the SNP-triglyceride-to-lipid ratio association (*x*-axis, SD units) and the SNP-GM-BAG associations (*y*-axis, log OR) with standard error bars. The slopes of the purple and green lines correspond to the causal effect sizes estimated by the IVW and the MR Egger estimator, respectively. We annotated a potential outlier. **E**) Funnel plot for the relationship between the causal effect of the triglyceride-to-lipid ratio on GM-BAG. Each dot represents MR effect sizes estimated using each SNP as a separate instrument against the inverse of the standard error of the causal estimate. The vertical red line shows the MR estimates using all SNPs. We annotated a potential outlier. Abbreviation: AD: Alzheimer's disease; AST: aspartate aminotransferase; BMI: body mass

434 index; VLDL: very low-density lipoprotein; CI: confidence interval; OR: odds ratio; SD:
435 standard deviation; SE: standard error.
436

Discussion

The present study harnessed brain imaging genetics from a cohort of 42,089 participants in UKBB to investigate the underlying genetics of multimodal BAG. Our approach commenced with objectively assessing brain age prediction performance, encompassing various imaging modalities (T1-weighted, diffusion, and resting-state MRI), feature types (ROI vs. voxel), and machine learning algorithms. Subsequently, we conducted genome-wide associations, demonstrating the robustness of identified genetic signals in individuals of European ancestry across diverse factors. Lastly, our study encompassed several post-GWAS analyses, validating the GWAS results, shedding light on the intricate biological processes involved, and uncovering the multifaceted interplay between human brain aging and various health conditions and clinical traits. Our findings unveiled shared genetic factors and unique characteristics – varying degrees of phenotypic and genetic correlation – within BAG across three distinct imaging modalities.

Genetic architecture of GM-BAG

Our genetic results from GM-BAG substantiate that many diseases, conditions, and clinical phenotypes share genetic underpinnings with brain age, perhaps driven by macrostructural changes in GM (e.g., brain atrophy). The locus with the most significant signal (the top lead SNP rs534114641 at 17q21.31) showed substantial association with the traits mentioned above and was mapped to numerous genes associated with various diseases (**Fig. 2C**). Several previous GM-BAG GWAS[20,22] also identified this locus. Among these genes, the *MAPT* gene, known to encode a protein called tau, is a prominent AD hallmark and implicated in approximately 30 tauopathies, including progressive supranuclear palsy and frontotemporal lobar degeneration[68]. Our gene-drug-disease network also showed several drugs, such as Semorinemab[44], in active clinical trials currently targeting treatment for AD (**Fig. 3**). The

heritability enrichment of GM-BAG was high in several functional categories, with conserved regions being the most prominent. The observed higher heritability enrichment in conserved regions compared to coding regions[69] supports the long-standing hypothesis regarding the functional significance of conserved sequences. However, the precise role of many highly conserved non-coding DNA sequences remains unclear[70]. The genetic correlation results of GM-BAG with subtypes of common brain diseases highlight the promise for the AI-derived subtypes, rather than the "one-for-all" unitary disease diagnosis, as robust endophenotypes[23]. These findings strongly support the clinical implications of re-evaluating pertinent hypotheses using the AI-derived subtypes in patient stratification and personalized medicine.

The elevated triglyceride-to-lipid ratio in VLDL, an established biomarker for cardiovascular diseases[71], is causally associated with higher GM-BAG (accelerated brain age). Therefore, lifestyle interventions that target this biomarker might hold promise as an effective strategy to enhance overall brain health. In addition, we revealed that one unit-increased likelihood of type 2 diabetes has a causal effect on GM-BAG increase. Research has shown that normal brain aging is accelerated by approximately 26% in patients with progressive type 2 diabetes compared with healthy controls[72]. The protective causal effect of breast cancer on GM-BAG is intriguing in light of existing literature adversely linking breast cancer to brain metastasis[73] and chemotherapy-induced cognitive impairments, commonly known as "chemo brain". In addition, it's important to exercise caution when considering the potential causal link between breast cancer and GM-BAG, as MR analyses are susceptible to population selection bias[74] due to the high breast cancer mortality rate.

Genetic architecture of WM-BAG

The genetic architecture of WM-BAG exhibits strong correlations with cancer-related traits, AD, and physical measures such as BMI, among others. Our phenome-wide association query largely confirms the enrichment of these traits in previous literature. In particular, the *DNAJC1* gene, annotated from the most polygenic locus on chromosome 10 (top lead SNP: rs564819152), encodes a protein called heat shock protein 40 (Hsp40) and plays a role in protein folding and the response to cellular stress. This gene is implicated in various cancer types, such as breast, renal, and melanoma (**Supplementary eFigure 12**). In addition, several FDA-approved drugs have been developed based on these WM-BAG genes for different types of cancer in our gene-drug-disease network (**Fig. 3**). Our findings provide novel insights into the genetic underpinnings of WM-BAG and their potential relevance to cancer.

Remarkably, one unit-increased likelihood of AD was causally associated with increased WM-BAG. Our Mendelian randomization analysis confirmed the abundant association evidenced by the phenome-wide association query (**Fig. 2B**). Dementia, such as AD, is undeniably a significant factor contributing to the decline of the aging brain. Evidence suggests that AD is not solely a GM disease; significant microstructural changes can be observed in WM before the onset of cognitive decline[75]. We also identified a nominal causal significance of BMI [risk effect; P-value=4.73×10^{-2}, OR (95% CI) = 1.03 (1.00, 1.07)] on WM-BAG. These findings underscore the potential of lifestyle interventions and medications currently being tested in clinical trials for AD to improve overall brain health.

Genetic architecture of FC-BAG

The genetic signals for FC-BAG were weaker than those observed for GM and WM-BAG, which is consistent with the age prediction performance and partially corroborates Cheverud's conjecture: using genetic correlations (**Fig. 2F**) as proxies for phenotypic correlations

(**Fig. 1E**) when collecting individual phenotypes is expensive and unavailable. A novel genomic locus on chromosome 6 (6q.13) harbors an independent variant (rs1204329) previously linked to insomnia[76]. The top lead SNP, rs5877290, associated with this locus is a novel deletion-insertion mutation type: no known association with any human disease or gene mapping has been established for this SNP. The genetic basis of FC-BAG covaries with educational performance and schizophrenia subtypes. Specifically, parental education has been linked to cognitive ability, and researchers have identified a functional connectivity biomarker between the right rostral prefrontal cortex and occipital cortex that mediates the transmission of maternal education to offspring's performance IQ[77]. On the other hand, schizophrenia is a highly heritable mental disorder that exhibits functional dysconnectivity throughout the brain[78]. AD was causally associated with FC-BAG with nominal significance [risk effect for per unit increase; P-value=4.43×10^{-2}, OR (95% CI) = 1.02 (1.00, 1.03), number of SNPs=13] (**Fig. 5A**). The relationship between functional brain networks and the characteristic distribution of amyloid-β and tau in AD[79] provides evidence that AD is a significant factor in the aging brain, underscoring its role as a primary causative agent.

The comparative trend of genetic heritability among GM, WM, and FC-BAG is also consistent with previous large-scale GWAS of multimodal brain IDP. Zhao et al. performed GWAS on GM[13], WM[14], and FC-IDP[18], showing that FC-IDP is less genetically heritable than others. Similar observations were also demonstrated by Elliot et al.[11] in the first large-scale GWAS using multimodal IDP from UKBB. The weaker genetic signal observed in FC-BAG can be attributed to many factors. One of the main reasons is the higher signal-to-noise ratio in FC measurements due to the dynamic and complex nature of brain activity, which can make it difficult to accurately measure and distinguish between the true signal and noise. Social-

528 environmental and lifestyle factors can also contribute to the "missing heritability" observed in
529 FC-BAG. For example, stress, sleep patterns, physical activity, and other environmental factors
530 can impact brain function and connectivity[80]. In contrast, GM and WM measurements are more
531 stable and less influenced by environmental factors, which may explain why they exhibit
532 stronger genetic signals and higher heritability estimates.
533
534 **Limitations**
535 This study has several limitations. We can employ deep learning on voxel-wise imaging scans to
536 enhance brain age prediction performance. Nevertheless, it warrants additional exploration to
537 determine whether the resulting reduction in MAE translates into more robust genome-wide
538 associations, as our previous work has demonstrated that BAGs derived from a CNN with a
539 lower MAE did not exhibit heightened sensitivity to disease effects such as AD[35]. Second, the
540 generalization ability of the GWAS findings to non-European ancestry is limited, potentially due
541 to small sample sizes and cryptic population stratification. Future investigations can be expanded
542 to encompass a broader spectrum of underrepresented ethnic groups, diverse disease populations,
543 and various age ranges spanning the entire lifespan. This expansion can be facilitated by
544 leveraging the resources of large-scale brain imaging genetic consortia like ADNI[81], focused on
545 Alzheimer's disease, and ABCD[82], which centers on brain development during adolescence.
546 Third, it's important to exercise caution when interpreting the results of this study due to the
547 various assumptions associated with the statistical methods employed, including LDSC and MR.
548 Lastly, it's worth noting that brain age represents a residual score encompassing measurement
549 error. A recent study[83] has underscored the significance of incorporating longitudinal data when

calculating brain age. Future research should be conducted once the longitudinal scans from the UK Biobank become accessible to explore this impact on GWASs.

Outlook

In summary, our multimodal BAG GWASs provide evidence that the aging process of the human brain is a complex biological phenomenon intertwined with several organ systems and chronic diseases. We digitized the human brain from multimodal imaging and captured a complete genetic landscape of human brain aging. This opens new avenues for drug repurposing/repositioning and aids in identifying modifiable protective and risk factors that can ameliorate human brain health.

Methods

Method 1: Study populations

UKBB is a population-based study of more than 50,000 people recruited between 2006 and 2010 from Great Britain. The current study focused on participants from the imaging-genomics population who underwent both an MRI scan and genome sequencing (genotype array data and the imputed genotype data) under application number 35148. The UKBB study has ethical approval, and the ethics committee is detailed here: https://www.ukbiobank.ac.uk/learn-more-about-uk-biobank/governance/ethics-advisory-committee. The study design, phenotype and genetic data availability, and quality check have been published and detailed elsewhere[24]. **Table 1** shows the study characteristics of the present work.

To train the machine learning model and compare the performance of the multimodal BAG, we defined the following two datasets:

- *Training/validation/test dataset*: To objectively compare the age prediction performance of different MRI modalities and machine learning models, we randomly sub-sampled 500 (250 females) participants within each decade's range from 44 to 84 years old, resulting in the same 4000 participants for GM, WM, and FC-IDP. This dataset was used to train machine learning models. In addition, we ensured that the training/validation/test splits were the same in the CV procedure. As UKBB is a general population, we explicitly excluded participants with common brain diseases, including mental and behavioral disorders (ICD-10 code: F; *N*=2678) and diseases linked to the central nervous system (ICD-10 code: G group; *N*=3336).

- *Independent test dataset*: The rest of the population for each MRI modality (*N*=38089) was set as independent test datasets – unseen until we finalized the training procedure[84].

The GM-IDP includes 119 GM regional volumes from the MUSE atlas, consolidated by the iSTAGING consortium. We studied the influence of different WM-IDP features: i) 48 FA values; ii) 109 TBSS-based[85] values from FA, MD, ODI, and NDI; iii) 192 skeleton-based mean values from FA, MD, ODI, and NDI. For FC-IDP, 210 ICA-derived functional connectivity components were included. The WM and FC-IDP were downloaded from UKBB (**Method 3B**).

Table 1. Study characteristics.
The current table presents participants of all ancestries for the age prediction task. We constrained participants with only European ancestry for downstream genetic analyses. * For age and sex, we reported statistics for the overlapping population of the three modalities: 35,261 participants for the entire population, 4000 participants for the training/validation/test dataset, and 31,261 participants for the independent test dataset. We also showed the number of participants for the GM, WM, and FC-BAG GWAS. In total, our analyses included 42,089 unique participants who had at least one image scan. Abbreviation: dMRI: diffusion MRI; rsfMRI: resting-state functional MRI; T1w MRI: T1-weighted MRI.

Population (overlap)	T1w MRI	dMRI	rsfMRI	Age (year)*	Sex /female*
Total (35,261)	36,304	39,661	36,858	63.64 (45.00, 81.00)	18,700/53%
Training/validation/test (4000)	4000	4000	4000	63.47 (46.00, 81.00)	2000/50%
Independent test (31,261)	32,304	35,661	32,858	63.66 (45.00, 81.00)	16,700/53%
GWAS	31,557	31,749	32,017	NA	NA

Method 2: Image processing

(A): T1-weighted MRI processing: The imaging quality check is detailed in **Supplementary eMethod 2**. All images were first corrected for magnetic field intensity inhomogeneity.[86] A deep

learning-based skull stripping algorithm was applied to remove extra-cranial material. In total, 145 IDPs were generated in gray matter (GM, 119 ROIs), white matter (WM, 20 ROIs), and ventricles (6 ROIs) using a multi-atlas label fusion method[41]. The 119 GM ROIs were fit to the four machine learning models to derive the GM-BAG.

(B): Diffusion MRI processing: UKBB has processed diffusion MRI (dMRI) data and released several WM tract-based metrics for the Diffusion Tensor Imaging (DTI) model (single-shell dMRI) and Neurite Orientation Dispersion and Density Imaging (NODDI[87]) model (multi-shell dMRI). The Eddy[88] tool corrected raw images for eddy currents, head motion, and outlier slices. The mean values of FA, MD, ODI, and NDI were extracted from the 48 WM tracts of the "ICBM-DTI-81 white-matter labels" atlas[89], resulting in 192 WM-IDP (category code:134). In addition, a tract-skeleton (TBSS)[85] and probabilistic tractography analysis[90] were employed to derive weighted-mean measures within the 27 major WM tracts, referred to as the 108 TBSS WM-IDP (category code: 135). Finally, since we observed overfitting – an increase of MAEs from the cross-validated test results to the independent test results – when incorporating features from FA, MD, ODI, and NDI (as detailed in **Supplementary eTable 1A**), we chose to use only the 48 FA WM-IDPs to train the models for generating GM-BAG.

(C): Resting-state functional MRI processing: For FC-IDP, we used the 21 × 21 resting-state functional connectivity (full correlation) matrices (data-field code: 25750) from UKBB[91,92]. UKBB processed rsfMRI data and released 25 whole-brain spatial independent component analysis (ICA)-derived components[93]; four components were removed due to artifactual components. This resulted in 210 FC-IDP quantifying pairwise correlations of the ICA-derived

components. Details of dMRI and rsfMRI processing are documented here: https://biobank.ctsu.ox.ac.uk/crystal/crystal/docs/brain_mri.pdf.

Method 3: Multimodal brain age prediction using machine learning models

GM, WM, and FC-IDP (details of image processing are presented in **Method 2**) were fit into four machine learning models (linear and non-linear) to predict brain age as the outcome. Specifically, we used SVR, LASSO regression, MLP, and a five-layer neural network (NN: three linear layers and one rectified linear unit layer).

To objectively and reproducibly compare the age prediction performance using different machine learning models and MRI modalities, we adopted a nested CV procedure and included an independent test dataset[27]. Specifically, the outer loop CV was performed for 100 repeated random splits: 80% of the data were used for training. The remaining 20% was used for validation/testing in the inner loop with a 10-fold CV. In addition, we concealed an independent test dataset – unseen for testing until we finished fine-tuning the machine learning models[84] (e.g., hyperparameters for SVR and neural networks). To compare the results of different models and modalities, we showed MAE's mean and empirical standard deviation instead of performing any statistical test (e.g., a two-sample t-test). This is because no unbiased variance estimate exists for complex CV procedures (refer to notes from Nadeau and Benjio[94]).

Method 4: Genetic analyses

Imputed genotype data were quality-checked for downstream analyses. Our quality check pipeline (see below**)** resulted in 33,541 European ancestry participants and 8,469,833 SNPs. After merging with the multimodal MRI populations, we included 31,557 European participants

for GM-BAG, 31,749 participants for WM-BAG, and 32,017 participants for FC-BAG GWAS. Details of the protocol are described elsewhere[15,95]. We summarize our genetic QC pipeline as below. First, we excluded related individuals (up to 2nd-degree) from the complete UKBB sample using the KING software for family relationship inference[96]. We then removed duplicated variants from all 22 autosomal chromosomes. Individuals whose genetically identified sex did not match their self-acknowledged sex were removed. Other excluding criteria were: i) individuals with more than 3% of missing genotypes; ii) variants with minor allele frequency (MAF) of less than 1%; iii) variants with larger than 3% missing genotyping rate; iv) variants that failed the Hardy-Weinberg test at $1x10^{-10}$. To adjust for population stratification[97], we derived the first 40 genetic principle components (PC) using the FlashPCA software[98]. Details of the genetic quality check protocol are described elsewhere[95,99].

(A): Genome-wide association analysis: For GWAS, we ran a linear regression using Plink[100] for GM, WM, and FC-BAG, controlling for confounders of age, dataset status (training/validation/test or independent test dataset), age x squared, sex, age x sex interaction, age-squared x sex interaction, total intracranial volume, the brain position in the scanner (lateral, transverse, and longitudinal), and the first 40 genetic principal components. The inclusion of these covariates is guided by pioneer neuroimaging GWAS conducted by Zhao et al[13]. and Elliot et al.[11] We adopted the genome-wide P-value threshold (5×10^{-8}) and annotated independent genetic signals considering linkage disequilibrium (see below). We then estimated the SNP-based heritability using GCTA[37] using the individual-level genotype data with the same covariates in GWAS.

672 To check the robustness of our GWAS results using European ancestry, we performed six
673 sensitivity checks, including *i*) split-sample GWAS by randomly dividing the entire population
674 into two sex and age-matched splits, *ii*) sex-stratified GWAS for males and females, *iii*) non-
675 European GWAS, *iv*) fastGWA[40] for a mixed linear model that accounts for cryptic population
676 stratification, *v*) machine learning-specific GWAS, and *vi*) feature type-specific GWAS.
677
678 **(B): Annotation of genomic loci and genes**: The annotation of genomic loci and mapped genes
679 was performed via FUMA[101] (https://fuma.ctglab.nl/, version: v1.5.0). For the annotation of
680 genomic loci, we first defined lead SNPs (correlation $r^2 \leq 0.1$, distance < 250 kilobases) and
681 assigned them to a genomic locus (non-overlapping); the lead SNP with the lowest P-value (i.e.,
682 the top lead SNP) was used to represent the genomic locus. For gene mappings, three different
683 strategies were considered. First, positional mapping assigns the SNP to its physically nearby
684 genes (a 10 kb window by default). Second, eQTL mapping annotates SNPs to genes based on
685 eQTL associations. Finally, chromatin interaction mapping annotates SNPs to genes when there is
686 a significant chromatin interaction between the disease-associated regions and nearby or distant
687 genes.[101] The definition of top lead SNP, lead SNP, independent significant SNP, and candidate
688 SNP can be found in **Supplementary eMethod 1**.
689
690 **(C): Phenome-wide association query for genomic loci associated with other traits in the**
691 **literature**: We queried the significant independent SNPs within each locus in the GWAS
692 Catalog (query date: January 10th, 2023 via FUMA version: v1.5.0) to determine their
693 previously identified associations with other traits. For these associated traits, we further mapped
694 them into several high-level categories for visualization purposes (**Fig. 2B**).

695

696 **(D): Genetic correlation**: We used LDSC[36] to estimate the pairwise genetic correlation (r_g)
697 between GM, WM, and FC-BAG and several pre-selected traits (**Supplementary eTable 3**) by
698 using the precomputed LD scores from the 1000 Genomes of European ancestry. The following
699 pre-selected traits were included: Alzheimer's disease (AD), autism spectrum disorder (ASD),
700 attention-deficit/hyperactivity disorder (ADHD), obsessive-compulsive disorder (OCD), major
701 depressive disorder (MDD), bipolar disorder (BIP), schizophrenia (SCZ), education and
702 intelligence, as well as the AI-derived subtypes for AD (AD1 and AD2[102]), ASD (ASD1, ASD2,
703 and ASD3[47]), and SCZ (SCZ1 and SCZ2[103]) – serving as more robust endophenotypes than the
704 disease diagnoses themselves. To ensure the suitability of the GWAS summary statistics, we first
705 checked that the selected study's population was European ancestry; we then guaranteed a
706 moderate SNP-based heritability h^2 estimate and excluded the studies with spurious low h^2
707 (<0.05). Notably, LDSC corrects for sample overlap and provides an unbiased estimate of
708 genetic correlation[104]. The h^2 estimate from LDSC is, in general, lower than that of GCTA
709 because LDSC uses GWAS summary statistics and pre-computed LD information and has
710 slightly different model assumptions across different software[105].

711

712 **(E): Partitioned heritability estimate**: Partitioned heritability analysis estimates the percentage
713 of heritability enrichment explained by annotated genome regions[51]. First, the partitioned
714 heritability was calculated for 53 main functional categories. The 53 functional categories are not
715 specific to any cell type, including coding, UTR, promoter, and intronic regions. Details of the
716 53 categories are described elsewhere[51] and are also presented in **Supplementary eTable 5A**.
717 Subsequently, cell type-specific partitioned heritability was estimated using gene sets from

718 Cahoy et al.[58] for three main cell types (i.e., astrocyte, neuron, and oligodendrocyte)
719 (**Supplementary eTable 5B)**.
720
721 **(F): Gene-drug-disease network construction**: We curated data from the Drug Bank database
722 (v.5.1.9)[106] and the Therapeutic Target Database (updated by September 29th, 2021) to construct
723 a gene-drug-disease network. Specifically, we constrained the target to human organisms and
724 included all drugs with active statuses (e.g., patented and approved) but excluded inactive ones
725 (e.g., terminated or discontinued at any phase). To represent the disease, we mapped the
726 identified drugs to the Anatomical Therapeutic Chemical (ATC) classification system for the
727 Drugbank database and the International Classification of Diseases (ICD-11) for the Therapeutic
728 Target Database.
729
730 **(G): Two-sample Mendelian Randomization**: We investigated whether the clinical traits
731 previously associated with our genomic loci (**Fig. 2B**) were a cause or a consequence of GM,
732 WM, and FC-BAG using a bidirectional, two-sample MR approach. GM, WM, and FC-BAG are
733 the outcome/exposure variables in the forward/inverse MR, respectively. We applied five
734 different MR methods using the TwoSampleMR R package[59], including the inverse variance
735 weighted (IVW), MR Egger[107], weighted median[108], simple mode, and weighted mode methods.
736 We reported the results of IVW in the main text and the four others in the **Supplementary eFile**
737 **9**. MR relies on a set of crucial assumptions to ensure the validity of its results. These
738 assumptions include the requirement that the chosen genetic instrument exhibits a strong
739 association with the exposure of interest while remaining free from direct associations with
740 confounding factors that could influence the outcome. Additionally, the genetic variant used in

MR should be independently allocated during conception and inheritance, guaranteeing its autonomy from potential confounders. Furthermore, this genetic instrument must affect the outcome solely through the exposure of interest without directly impacting alternative pathways that could influence the outcome (no horizontal pleiotropy). The five MR methods handle pleiotropy and instrument validity assumptions differently, offering various degrees of robustness to violations. For example, MR Egger provides a method to estimate and correct for pleiotropy, making it robust in the presence of horizontal pleiotropy. However, it assumes that directional pleiotropy is the only form of pleiotropy present.

To ensure an unbiased selection of exposure variables, we followed a systematic procedure guided by the STROBE-MR Statement[109]. We pre-selected exposure variables across various categories based on our phenome-wide association query. These variables encompassed neurodegenerative diseases (e.g., AD), liver biomarkers (e.g., AST), cardiovascular diseases (e.g., the triglyceride-to-lipid ratio in VLDL), and lifestyle-related risk factors (e.g., BMI). Subsequently, we conducted an automated query for these traits in the IEU GWAS database[110], which provides curated GWAS summary statistics suitable for MR, using the *available_outcomes()* function. We ensured the selected studies used European ancestry populations and shared the same genome build as our GWAS (HG19/GRCh37). Additionally, we manually examined the selected studies to exclude any GWAS summary statistics overlapping with UK Biobank populations to prevent bias stemming from sample overlap[111]. This process yielded a set of seven exposure variables, comprising AD, breast cancer, type 2 diabetes, renin level, triglyceride-to-lipid ratio, aspartate aminotransferase (AST), and BMI. The details of the selected studies for the instrumental variables (IVs) are provided in **Supplementary eTable 6**.

We performed several sensitivity analyses. First, a heterogeneity test was performed to check for violating the IV assumptions. Horizontal pleiotropy was estimated to navigate the violation of the IV's exclusivity assumption[64] using a funnel plot, single-SNP MR approaches, and MR Egger estimator[107]. Moreover, the leave-one-out analysis excluded one instrument (SNP) at a time and assessed the sensitivity of the results to individual SNP.

(H): PRS prediction: We calculated the PRS using the GWAS results from the split-sample analyses. The weights of the PRS were defined based on split1 data (training/base data), and the split2 GWAS summary statistics were used as the test/target data. The QC steps for the base data are as follows: *i*) removal of duplicated and ambiguous SNPs for the base data; *ii*) clumping the base GWAS data; *iii*) pruning to remove highly correlated SNPs in the target data; *iv*) removal of high heterozygosity samples in the target data; *v*) removal of duplicated, mismatching and ambiguous SNPs in the target data. After rigorous QC, we employed two methods to derive the three BAG-PRS in the split2 population: *i*) PLINK with the classic C+T method (clumping + thresholding) and *ii*) PRS-CS[57] with a Bayesian approach.

To determine the "best-fit" PRS P-value threshold, we performed a linear regression using the PRS calculated at different P-value thresholds (0.001, 0.05, 0.1, 0.2, 0.3, 0.4, 0.5), controlling for age, sex, total intracellular volume, brain position during scanning (lateral, transverse, and longitudinal), and the first forty genetic PCs. A null model was established by including only the abovementioned covariates. The alternative model was then constructed by introducing each BAG-PRS as an extra independent variable.

Data Availability

The GWAS summary statistics corresponding to this study are publicly available on the MEDICINE knowledge portal (https://labs.loni.usc.edu/medicine).

Code Availability

The software and resources used in this study are all publicly available:

- MLNI: https://anbai106.github.io/mlni/, brain age prediction (V0.1.2)
- MEDICINE: https://labs.loni.usc.edu/medicine, knowledge portal for dissemination and GWAS summary statistics sharing
- MUSE: https://www.med.upenn.edu/sbia/muse.html, image preprocessing for GM-IDP
- PLINK: https://www.cog-genomics.org/plink/, GWAS and PRS
- FUMA: https://fuma.ctglab.nl/, gene mapping, genomic locus annotation
- GCTA: https://yanglab.westlake.edu.cn/software/gcta/#Overview, heritability estimates, and fastGWA
- LDSC: https://github.com/bulik/ldsc, genetic correlation, partitioned heritability
- TwoSampleMR: https://mrcieu.github.io/TwoSampleMR/index.html, MR
- PRS-CS: https://github.com/getian107/PRScs, PRS

Competing Interests

None

Authors' contributions

Dr. Wen has full access to all the data in the study and takes responsibility for the integrity of the data and the accuracy of the data analysis.

Study concept and design: Wen

Acquisition, analysis, or interpretation of data: Wen

Drafting of the manuscript: Wen

Critical revision of the manuscript for important intellectual content: all authors

Statistical analysis: Wen

References

1. Rajpurkar, P., Chen, E., Banerjee, O. & Topol, E. J. AI in health and medicine. *Nat Med* **28**, 31–38 (2022).

2. Hassabis, D., Kumaran, D., Summerfield, C. & Botvinick, M. Neuroscience-Inspired Artificial Intelligence. *Neuron* **95**, 245–258 (2017).

3. Lee, J. *et al.* Deep learning-based brain age prediction in normal aging and dementia. *Nat Aging* **2**, 412–424 (2022).

4. Wen, J. *et al.* Genetic, clinical underpinnings of subtle early brain change along Alzheimer's dimensions. 2022.09.16.508329 Preprint at https://doi.org/10.1101/2022.09.16.508329 (2022).

5. Hollon, T. *et al.* Artificial-intelligence-based molecular classification of diffuse gliomas using rapid, label-free optical imaging. *Nat Med* 1–5 (2023) doi:10.1038/s41591-023-02252-4.

6. Cole, J. H., Marioni, R. E., Harris, S. E. & Deary, I. J. Brain age and other bodily 'ages': implications for neuropsychiatry. *Mol Psychiatry* **24**, 266–281 (2019).

7. Jones, D. T., Lee, J. & Topol, E. J. Digitising brain age. *The Lancet* **400**, 988 (2022).

8. Tian, Y. E. *et al.* Heterogeneous aging across multiple organ systems and prediction of chronic disease and mortality. *Nat Med* 1–11 (2023) doi:10.1038/s41591-023-02296-6.

9. Kaufmann, T. *et al.* Common brain disorders are associated with heritable patterns of apparent aging of the brain. *Nat Neurosci* **22**, 1617–1623 (2019).

10. Shen, L. & Thompson, P. M. Brain Imaging Genomics: Integrated Analysis and Machine Learning. *Proceedings of the IEEE* **108**, 125–162 (2020).

11. Elliott, L. T. *et al.* Genome-wide association studies of brain imaging phenotypes in UK Biobank. *Nature* **562**, 210–216 (2018).

12. Smith, S. M. *et al.* An expanded set of genome-wide association studies of brain imaging phenotypes in UK Biobank. *Nat Neurosci* **24**, 737–745 (2021).

13. Zhao, B. *et al.* Genome-wide association analysis of 19,629 individuals identifies variants influencing regional brain volumes and refines their genetic co-architecture with cognitive and mental health traits. *Nat Genet* **51**, 1637–1644 (2019).

14. Zhao, B. *et al.* Common genetic variation influencing human white matter microstructure. *Science* **372**, (2021).

15. Wen, J. *et al.* Novel genomic loci and pathways influence patterns of structural covariance in the human brain. 2022.07.20.22277727 Preprint at https://doi.org/10.1101/2022.07.20.22277727 (2022).

16. Grasby, K. L. *et al.* The genetic architecture of the human cerebral cortex. *Science* **367**, eaay6690 (2020).

17. Brouwer, R. M. *et al.* Genetic variants associated with longitudinal changes in brain structure across the lifespan. *Nat Neurosci* **25**, 421–432 (2022).

18. Zhao, B. *et al.* Common variants contribute to intrinsic human brain functional networks. *Nat Genet* **54**, 508–517 (2022).

19. Smith, S. M. *et al.* Brain aging comprises many modes of structural and functional change with distinct genetic and biophysical associations. *eLife* **9**, e52677.

20. Ning, K. *et al.* Improving brain age estimates with deep learning leads to identification of novel genetic factors associated with brain aging. *Neurobiology of Aging* **105**, 199–204 (2021).

21. Leonardsen, E. H. *et al.* Genetic architecture of brain age and its causal relations with brain and mental disorders. *Mol Psychiatry* 1–10 (2023) doi:10.1038/s41380-023-02087-y.

22. Jonsson, B. A. *et al.* Brain age prediction using deep learning uncovers associated sequence variants. *Nat Commun* **10**, 5409 (2019).

23. Kendler, K. & Neale, M. Endophenotype: a conceptual analysis. *Mol Psychiatry* **15**, 789–797 (2010).

24. Bycroft, C. *et al.* The UK Biobank resource with deep phenotyping and genomic data. *Nature* **562**, 203–209 (2018).

25. Emdin, C. A., Khera, A. V. & Kathiresan, S. Mendelian Randomization. *JAMA* **318**, 1925–1926 (2017).

26. Varoquaux, G. *et al.* Assessing and tuning brain decoders: Cross-validation, caveats, and guidelines. *NeuroImage* **145**, 166–179 (2017).

27. Samper-González, J. *et al.* Reproducible evaluation of classification methods in Alzheimer's disease: Framework and application to MRI and PET data. *NeuroImage* **183**, 504–521 (2018).

28. Pedregosa, F. *et al.* Scikit-learn: Machine Learning in Python. *J. Mach. Learn. Res.* **12**, 2825–2830 (2011).

29. de Lange, A.-M. G. & Cole, J. H. Commentary: Correction procedures in brain-age prediction. *Neuroimage Clin* **26**, 102229 (2020).

30. Peng, H., Gong, W., Beckmann, C. F., Vedaldi, A. & Smith, S. M. Accurate brain age prediction with lightweight deep neural networks. *Medical Image Analysis* **68**, 101871 (2021).

878 31. Leonardsen, E. H. *et al.* Deep neural networks learn general and clinically relevant
879 representations of the ageing brain. *NeuroImage* **256**, 119210 (2022).
880 32. Vidal-Pineiro, D. *et al.* Individual variations in 'brain age' relate to early-life factors more
881 than to longitudinal brain change. *eLife* **10**, e69995 (2021).
882 33. Wood, D. A. *et al.* Accurate brain-age models for routine clinical MRI examinations.
883 *Neuroimage* **249**, 118871 (2022).
884 34. More, S. *et al.* Brain-age prediction: A systematic comparison of machine learning
885 workflows. *NeuroImage* **270**, 119947 (2023).
886 35. Bashyam, V. M. *et al.* MRI signatures of brain age and disease over the lifespan based on a
887 deep brain network and 14 468 individuals worldwide. *Brain* **143**, 2312–2324 (2020).
888 36. Bulik-Sullivan, B. K. *et al.* LD Score regression distinguishes confounding from
889 polygenicity in genome-wide association studies. *Nat Genet* **47**, 291–295 (2015).
890 37. Yang, J., Lee, S. H., Goddard, M. E. & Visscher, P. M. GCTA: A Tool for Genome-wide
891 Complex Trait Analysis. *Am J Hum Genet* **88**, 76–82 (2011).
892 38. Buniello, A. *et al.* The NHGRI-EBI GWAS Catalog of published genome-wide association
893 studies, targeted arrays and summary statistics 2019. *Nucleic Acids Res* **47**, D1005–D1012
894 (2019).
895 39. Cheverud, J. M. A COMPARISON OF GENETIC AND PHENOTYPIC
896 CORRELATIONS. *Evolution* **42**, 958–968 (1988).
897 40. Jiang, L. *et al.* A resource-efficient tool for mixed model association analysis of large-scale
898 data. *Nat Genet* **51**, 1749–1755 (2019).

41. Doshi, J. *et al.* MUSE: MUlti-atlas region Segmentation utilizing Ensembles of registration algorithms and parameters, and locally optimal atlas selection. *Neuroimage* **127**, 186–195 (2016).

42. Davatzikos, C., Genc, A., Xu, D. & Resnick, S. M. Voxel-Based Morphometry Using the RAVENS Maps: Methods and Validation Using Simulated Longitudinal Atrophy. *NeuroImage* **14**, 1361–1369 (2001).

43. Hopkins, A. L. & Groom, C. R. The druggable genome. *Nat Rev Drug Discov* **1**, 727–730 (2002).

44. Antibody-Mediated Targeting of Tau In Vivo Does Not Require Effector Function and Microglial Engagement - PubMed. https://pubmed.ncbi.nlm.nih.gov/27475227/.

45. Wilcock, G. K. *et al.* Potential of Low Dose Leuco-Methylthioninium Bis(Hydromethanesulphonate) (LMTM) Monotherapy for Treatment of Mild Alzheimer's Disease: Cohort Analysis as Modified Primary Outcome in a Phase III Clinical Trial. *J Alzheimers Dis* **61**, 435–457.

46. Wen, J. *et al.* Subtyping brain diseases from imaging data. Preprint at https://doi.org/10.48550/arXiv.2202.10945 (2022).

47. Hwang, G. *et al.* Assessment of Neuroanatomical Endophenotypes of Autism Spectrum Disorder and Association With Characteristics of Individuals With Schizophrenia and the General Population. *JAMA Psychiatry* (2023) doi:10.1001/jamapsychiatry.2023.0409.

48. Chand, G. B. *et al.* Two distinct neuroanatomical subtypes of schizophrenia revealed using machine learning. *Brain* **143**, 1027–1038 (2020).

49. International Obsessive Compulsive Disorder Foundation Genetics Collaborative (IOCDF-GC) and OCD Collaborative Genetics Association Studies (OCGAS). Revealing the

complex genetic architecture of obsessive-compulsive disorder using meta-analysis. *Mol Psychiatry* **23**, 1181–1188 (2018).

50. Rietveld, C. A. *et al.* GWAS of 126,559 individuals identifies genetic variants associated with educational attainment. *Science* **340**, 1467–1471 (2013).

51. Finucane, H. K. *et al.* Partitioning heritability by functional annotation using genome-wide association summary statistics. *Nat Genet* **47**, 1228–1235 (2015).

52. Hoffman, M. M. *et al.* Integrative annotation of chromatin elements from ENCODE data. *Nucleic Acids Res* **41**, 827–841 (2013).

53. Haberle, V. & Stark, A. Eukaryotic core promoters and the functional basis of transcription initiation. *Nat Rev Mol Cell Biol* **19**, 621–637 (2018).

54. Trynka, G. *et al.* Chromatin marks identify critical cell types for fine mapping complex trait variants. *Nat Genet* **45**, 124–130 (2013).

55. Barski, A. *et al.* High-Resolution Profiling of Histone Methylations in the Human Genome. *Cell* **129**, 823–837 (2007).

56. Choi, S. W., Mak, T. S.-H. & O'Reilly, P. F. Tutorial: a guide to performing polygenic risk score analyses. *Nat Protoc* **15**, 2759–2772 (2020).

57. Ge, T., Chen, C.-Y., Ni, Y., Feng, Y.-C. A. & Smoller, J. W. Polygenic prediction via Bayesian regression and continuous shrinkage priors. *Nat Commun* **10**, 1776 (2019).

58. Cahoy, J. D. *et al.* A Transcriptome Database for Astrocytes, Neurons, and Oligodendrocytes: A New Resource for Understanding Brain Development and Function. *J. Neurosci.* **28**, 264–278 (2008).

59. Hemani, G. *et al.* The MR-Base platform supports systematic causal inference across the human phenome. *eLife* **7**, e34408 (2018).

945 60. Borges, M. C. *et al.* Circulating Fatty Acids and Risk of Coronary Heart Disease and
946 Stroke: Individual Participant Data Meta-Analysis in Up to 16 126 Participants. *J Am Heart*
947 *Assoc* **9**, e013131 (2020).
948 61. Morris, A. P. *et al.* Large-scale association analysis provides insights into the genetic
949 architecture and pathophysiology of type 2 diabetes. *Nat Genet* **44**, 981–990 (2012).
950 62. K, M. *et al.* Association analysis identifies 65 new breast cancer risk loci. *Nature* **551**,
951 (2017).
952 63. Lambert, J.-C. *et al.* Meta-analysis of 74,046 individuals identifies 11 new susceptibility
953 loci for Alzheimer's disease. *Nat Genet* **45**, 1452–1458 (2013).
954 64. Bowden, J. *et al.* A framework for the investigation of pleiotropy in two-sample summary
955 data Mendelian randomization. *Stat Med* **36**, 1783–1802 (2017).
956 65. Burgess, S. & Thompson, S. G. Interpreting findings from Mendelian randomization using
957 the MR-Egger method. *Eur J Epidemiol* **32**, 377–389 (2017).
958 66. Klarin, D. *et al.* Genetics of blood lipids among ~300,000 multi-ethnic participants of the
959 Million Veteran Program. *Nat Genet* **50**, 1514–1523 (2018).
960 67. Nelson, C. P. *et al.* Association analyses based on false discovery rate implicate new loci
961 for coronary artery disease. *Nat Genet* **49**, 1385–1391 (2017).
962 68. Horie, K. *et al.* CSF tau microtubule-binding region identifies pathological changes in
963 primary tauopathies. *Nat Med* **28**, 2547–2554 (2022).
964 69. Gusev, A. *et al.* Partitioning Heritability of Regulatory and Cell-Type-Specific Variants
965 across 11 Common Diseases. *The American Journal of Human Genetics* **95**, 535–552
966 (2014).

70. Stamatoyannopoulos, J. A. What does our genome encode? *Genome Res* **22**, 1602–1611 (2012).

71. Nordestgaard, B. G. & Varbo, A. Triglycerides and cardiovascular disease. *Lancet* **384**, 626–635 (2014).

72. Antal, B. *et al.* Type 2 diabetes mellitus accelerates brain aging and cognitive decline: Complementary findings from UK Biobank and meta-analyses. *Elife* **11**, e73138 (2022).

73. Wu, A. M. L. *et al.* Aging and CNS Myeloid Cell Depletion Attenuate Breast Cancer Brain Metastasis. *Clinical Cancer Research* **27**, 4422–4434 (2021).

74. Gkatzionis, A. & Burgess, S. Contextualizing selection bias in Mendelian randomization: how bad is it likely to be? *International Journal of Epidemiology* **48**, 691–701 (2019).

75. Sachdev, P. S., Zhuang, L., Braidy, N. & Wen, W. Is Alzheimer's a disease of the white matter? *Curr Opin Psychiatry* **26**, 244–251 (2013).

76. Watanabe, K. *et al.* Genome-wide meta-analysis of insomnia prioritizes genes associated with metabolic and psychiatric pathways. *Nat Genet* **54**, 1125–1132 (2022).

77. Cermakova, P. *et al.* Parental education, cognition and functional connectivity of the salience network. *Sci Rep* **13**, 2761 (2023).

78. Cao, H., Zhou, H. & Cannon, T. D. Functional connectome-wide associations of schizophrenia polygenic risk. *Mol Psychiatry* **26**, 2553–2561 (2021).

79. Yu, M., Sporns, O. & Saykin, A. J. The human connectome in Alzheimer disease — relationship to biomarkers and genetics. *Nat Rev Neurol* **17**, 545–563 (2021).

80. Tost, H., Champagne, F. A. & Meyer-Lindenberg, A. Environmental influence in the brain, human welfare and mental health. *Nat Neurosci* **18**, 1421–1431 (2015).

81. Petersen, R. C. *et al.* Alzheimer's Disease Neuroimaging Initiative (ADNI): clinical characterization. *Neurology* **74**, 201–209 (2010).

82. Casey, B. J. *et al.* The Adolescent Brain Cognitive Development (ABCD) study: Imaging acquisition across 21 sites. *Developmental Cognitive Neuroscience* **32**, 43–54 (2018).

83. Di Biase, M. A. *et al.* Mapping human brain charts cross-sectionally and longitudinally. *Proceedings of the National Academy of Sciences* **120**, e2216798120 (2023).

84. Wen, J. *et al.* Convolutional neural networks for classification of Alzheimer's disease: Overview and reproducible evaluation. *Medical Image Analysis* **63**, 101694 (2020).

85. Smith, S. M. *et al.* Tract-based spatial statistics: voxelwise analysis of multi-subject diffusion data. *Neuroimage* **31**, 1487–1505 (2006).

86. Tustison, N. J. *et al.* N4ITK: improved N3 bias correction. *IEEE Trans. Med. Imaging* **29**, 1310–1320 (2010).

87. Zhang, H., Schneider, T., Wheeler-Kingshott, C. A. & Alexander, D. C. NODDI: Practical in vivo neurite orientation dispersion and density imaging of the human brain. *NeuroImage* **61**, 1000–1016 (2012).

88. Smith, S. M. *et al.* Advances in functional and structural MR image analysis and implementation as FSL. *Neuroimage* **23 Suppl 1**, S208-19 (2004).

89. Mori, S., Wakana, S., Nagae-Poetscher, L. & van Zijl, P. *MRI Atlas of Human White Matter*. (Elsevier, 2005).

90. Wakana, S. *et al.* Reproducibility of quantitative tractography methods applied to cerebral white matter. *NeuroImage* **36**, 630–644 (2007).

91. Alfaro-Almagro, F. *et al.* Image processing and Quality Control for the first 10,000 brain imaging datasets from UK Biobank. *Neuroimage* **166**, (2018).

92. Miller, K. L. *et al.* Multimodal population brain imaging in the UK Biobank prospective epidemiological study. *Nature Neuroscience* **19**, 1523–1536 (2016).

93. Beckmann, C. F. & Smith, S. M. Probabilistic independent component analysis for functional magnetic resonance imaging. *IEEE Transactions on Medical Imaging* **23**, 137–152 (2004).

94. Inference for the Generalization Error | SpringerLink. https://link.springer.com/article/10.1023/A:1024068626366.

95. Wen, J. *et al.* Characterizing Heterogeneity in Neuroimaging, Cognition, Clinical Symptoms, and Genetics Among Patients With Late-Life Depression. *JAMA Psychiatry* (2022) doi:10.1001/jamapsychiatry.2022.0020.

96. Manichaikul, A. *et al.* Robust relationship inference in genome-wide association studies. *Bioinformatics* **26**, 2867–2873 (2010).

97. Price, A. L., Zaitlen, N. A., Reich, D. & Patterson, N. New approaches to population stratification in genome-wide association studies. *Nat Rev Genet* **11**, 459–463 (2010).

98. Abraham, G., Qiu, Y. & Inouye, M. FlashPCA2: principal component analysis of Biobank-scale genotype datasets. *Bioinformatics* **33**, 2776–2778 (2017).

99. Wen, J. *et al.* The Genetic Architecture of Biological Age in Nine Human Organ Systems. *medRxiv* 2023.06.08.23291168 (2023) doi:10.1101/2023.06.08.23291168.

100. Purcell, S. *et al.* PLINK: A Tool Set for Whole-Genome Association and Population-Based Linkage Analyses. *Am J Hum Genet* **81**, 559–575 (2007).

101. Watanabe, K., Taskesen, E., van Bochoven, A. & Posthuma, D. Functional mapping and annotation of genetic associations with FUMA. *Nat Commun* **8**, 1826 (2017).

1034 102. Wen, J. *et al.* Genetic, clinical underpinnings of subtle early brain change along
1035 Alzheimer's dimensions. 2022.09.16.508329 Preprint at
1036 https://doi.org/10.1101/2022.09.16.508329 (2022).
1037 103. Chand, G. B. *et al.* Two distinct neuroanatomical subtypes of schizophrenia revealed using
1038 machine learning. *Brain* **143**, 1027–1038 (2020).
1039 104. Bulik-Sullivan, B. *et al.* An atlas of genetic correlations across human diseases and traits.
1040 *Nat Genet* **47**, 1236–1241 (2015).
1041 105. Zhang, Y. *et al.* Comparison of methods for estimating genetic correlation between
1042 complex traits using GWAS summary statistics. *Brief Bioinform* **22**, bbaa442 (2021).
1043 106. Wishart, D. S. *et al.* DrugBank 5.0: a major update to the DrugBank database for 2018.
1044 *Nucleic Acids Res* **46**, D1074–D1082 (2018).
1045 107. Bowden, J., Davey Smith, G. & Burgess, S. Mendelian randomization with invalid
1046 instruments: effect estimation and bias detection through Egger regression. *Int J Epidemiol*
1047 **44**, 512–525 (2015).
1048 108. Bowden, J., Davey Smith, G., Haycock, P. C. & Burgess, S. Consistent Estimation in
1049 Mendelian Randomization with Some Invalid Instruments Using a Weighted Median
1050 Estimator. *Genet Epidemiol* **40**, 304–314 (2016).
1051 109. Skrivankova, V. W. *et al.* Strengthening the Reporting of Observational Studies in
1052 Epidemiology Using Mendelian Randomization: The STROBE-MR Statement. *JAMA* **326**,
1053 1614–1621 (2021).
1054 110. Elsworth, B. *et al.* The MRC IEU OpenGWAS data infrastructure. 2020.08.10.244293
1055 Preprint at https://doi.org/10.1101/2020.08.10.244293 (2020).

111. Burgess, S., Davies, N. M. & Thompson, S. G. Bias due to participant overlap in two-sample Mendelian randomization. *Genet Epidemiol* **40**, 597–608 (2016).

Acknowledgments

We want to express our sincere gratitude to the UK Biobank team for their invaluable contribution to advancing clinical research in our field. The primary funding support for this present study is from the initial funding package provided by Stevens Neuroimaging and Informatics Institute, Keck School of Medicine of USC, University of Southern California for WJ. The iSTAGING consortium is a multi-institutional effort funded by NIA by RF1 AG054409 for DC. This research has been conducted using the UK Biobank Resource under Application Number 35148. We thank Caroline O'Driscoll for her work creating the MEDICINE web portal, which has been instrumental in showcasing and disseminating our scientific findings.